Nano Res. 2011, 4(10): 948–962
DOI 10.1007/s12274-011-0151-8
Research Article

ISSN 1998-0124
CN 11-5974/O4

Cu_2O–Au Nanocomposites with Novel Structures and Remarkable Chemisorption Capacity and Photocatalytic Activity

Qing Hua[1,2,3], Fucheng Shi[1,2,3], Kai Chen[2], Sujie Chang[1,2,3], Yunsheng Ma[3], Zhiquan Jiang[1], Guoqiang Pan[4], and Weixin Huang[1,2,3] (✉)

[1] Hefei National Laboratory for Physical Sciences at the Microscale, University of Science and Technology of China, Hefei 230026, China
[2] CAS Key Laboratory of Materials for Energy Conversion, University of Science and Technology of China, Hefei 230026, China
[3] Department of Chemical Physics, University of Science and Technology of China, Hefei 230026, China
[4] National Synchrotron Radiation Laboratory, University of Science and Technology of China, Hefei 230029, China

Received: 9 May 2011 / Revised: 14 May 2011 / Accepted: 16 May 2011

ABSTRACT

The decomposition of CuH nanoparticles in aqueous solution has been successfully developed as a novel method for the preparation of Cu_2O nanoparticles. In particular, we found that the decomposition of CuH nanoparticles in aqueous solution could be catalyzed by Au colloids, forming Cu_2O–Au nanocomposites. The composition and structure of the resulting Cu_2O–Au nanocomposites have been characterized in detail by inductively coupled plasma atomic emission spectroscopy, powder X-ray diffraction, N_2 adsorption–desorption isotherms, infrared spectroscopy, X-ray photoelectron spectroscopy, scanning electron microscopy and transmission electron microscopy. Their visible-light-driven photocatalytic activity toward various dye molecules has also been investigated. Depending on the Au:Cu ratio, Cu_2O–Au nanocomposites exhibit different novel nanostructures including a beautiful flower-like nanostructure that consists of polycrystalline Cu_2O, amorphous Cu_2O and Au colloids. We propose that the rapidly-generated bubbles of H_2 during the course of the catalytic decomposition reaction drive the simultaneously-formed Cu_2O to form amorphous curved thin foils and might also act as a template to assemble curved thin foils of amorphous Cu_2O, polycrystalline Cu_2O and Au colloids into uniform nanostructures. A Cu_2O–Au nanocomposite with a Cu:Au ratio of 40 exhibits remarkable chemisorption capacity and visible-light-driven photocatalytic activity towards methyl orange and acid orange 7 and is a promising chemisorption–photocatalysis integrated catalyst. The catalytic decomposition of the metal hydride might open up a new approach for the fabrication of other metal/metal oxide nanocomposites with novel nanostructures and properties.

KEYWORDS

Cu_2O–Au nanocomposites, metal hydride, decomposition, chemisorption–photocatalysis integrated catalyst

1. Introduction

Cuprous oxide (Cu_2O) is a p-type semiconductor with a band gap of 2.0 eV which has attracted much interest due to its applications in optical and magnetic materials [1], solar energy conversion [2], gas sensing [3], lithium-ion batteries [4], and catalysis [5]. Recently the application of Cu_2O crystal as photocatalyst in

Address correspondence to huangwx@ustc.edu.cn

water splitting and organic contamination degradation under visible light illumination has been explored [6–16], but these systems still need further investigation. Hara et al. [6] first reported the photocatalytic decomposition of water into H_2 and O_2 on Cu_2O under visible light irradiation, but de Jongh et al. [7] pointed out that Cu_2O could be a promising material not just for direct photochemical water splitting but—in conjunction with a suitable redox system—as a p-type photoelectrode in an electrochemical photovoltaic cell. Later Hara et al. [8] also observed the generation of metallic Cu during water splitting on Cu_2O and proposed that a redox reaction between Cu and Cu_2O may be responsible for H_2 and O_2 formation in the Cu_2O-catalyzed overall water splitting. Cu_2O nanocrystals have also been reported to be active in the photodegradation of various dye molecules under visible light illumination [10–15], but Shi et al. [16] recently reported that Cu_2O nanowire polyhedra only exhibited photocatalytic activity for dye photodegradation in the presence of H_2O_2 under visible light irradiation.

Numerous Cu_2O nano- and micro-structures with well-controlled morphologies have been synthesized [17–35] and the shape of Cu_2O nanocrystals has been reported to exert a strong effect on their photocatalytic activity and stability in photocatalytic reactions [10–14]. Ho and Huang [12] reported that Cu_2O octahedra with exposed {111} crystal planes are active in the photocatalytic degradation of methyl orange (MO), whereas Cu_2O cubes with exposed {100} crystal planes are not, which was attributed to the fact that the Cu_2O(111) crystal plane contains surface copper atoms with dangling bonds. Similarly, Zhang et al. [11] also observed that Cu_2O octahedra exhibit a larger adsorption capacity toward MO than Cu_2O cubes. It was also reported that the {100} and {110} facets on Cu_2O crystals gradually disappear and transform into nanosheets with {111} facets during the photodegradation of MO [13]. Recently Zhang et al. [14] reported that 26-facet and 18-facet Cu_2O polyhedra with dominant {110} facets have a higher adsorption capacity and photocatalytic activity for the degradation of MO than Cu_2O octahedral with dominant {111} facets and cubes with {100} facets. The formation of Cu_2O–Au [36, 37], CuO–Cu_2O [38], and TiO_2–Cu_2O [39–41] nanocomposites has also been reported to enhance the photocatalytic activity under visible light irradiation.

Therefore, it is of interest to fabricate Cu_2O-based photocatalysts active under visible light irradiation and understand the underlying photocatalytic mechanism. In this paper, we report the synthesis of Cu_2O nanoparticles by the decomposition of CuH nanoparticles in aqueous solution. In particular, we found that the decomposition of CuH nanoparticles in aqueous solution could be catalyzed by Au colloids, readily forming Cu_2O–Au nanocomposites. Depending on the Cu:Au molar ratio, the resulting Cu_2O–Au nanocomposites exhibit a variety of morphologies including flower-like nanostructures. Interestingly, thin amorphous Cu_2O foils form in Cu_2O–Au nanocomposites with appropriate Cu:Au molar ratios. The Cu_2O–Au nanocomposite with a Cu:Au molar ratio of 40 (Cu_2O–Au-40) exhibits remarkable chemisorption capacities towards MO and acid orange 7 (AO 7), that reach 612 mg of MO and 751 mg of AO 7 per gram of Cu_2O–Au nanocomposite. It also exhibits good activity in the visible-light-driven photodegradation of MO and AO 7. Thus, Cu_2O–Au-40 nanocomposite is a promising chemisorption–photocatalysis integrated catalyst for the degradation of several dye molecules.

2. Experimental

2.1 Sample preparation

All the chemicals were analytical grade reagents and used as received without further purification. The CuH nanoparticles were synthesized by the reduction of $CuSO_4$ with H_3PO_2 at 45 °C [42] and filtered and washed several times with alcohol, and dried at room temperature in a vacuum oven. The decomposition of CuH nanoparticles in aqueous solution was then used to synthesize Cu_2O–Au nanocomposites. Typically, 20 mg of CuH was first ultrasonically dispersed in 40 mL of alcohol containing 0.6 g of dissolved poly(vinylpyrrolidone) (PVP) to prepare PVP-protected CuH nanoparticles. The PVP-protected CuH nanoparticles were added to 40 mL of deionized water containing 0.4 g of dissolved PVP, and then the calculated volume of $HAuCl_4$ aqueous solution (0.0932 mol/L) was added. The mixture was well stirred at room

temperature for 2.5 h. The precipitated Cu_2O–Au nanocomposite was separated from the solution by centrifugation, washed several times with alcohol, and dried at room temperature in a vacuum oven.

2.2 Sample characterization

Compositions of Cu_2O–Au nanocomposites were analyzed by means of inductively coupled plasma atomic emission spectroscopy (ICP-AES). Powder X-ray diffraction (XRD) experiments were performed on a Philips X'Pert PRO Super X-ray diffractometer equipped with a Ni-filtered Cu Kα X-ray source (λ = 1.541 874 Å). N_2 adsorption–desorption isotherms were measured on a Micromeritics ASAP 2020 M+C system. The pore size distribution of mesopores in the samples was analyzed with the Barrett–Joyner–Halenda (BJH) method. Infrared spectra were measured on a Nicolet 8700 Fourier transform infrared spectrometer with a spectral resolution of 4 cm^{-1}. High resolution X-ray photoelectron spectroscopy (XPS) measurements were performed on an ESCALAB 250 high performance electron spectrometer using a monochromated Al Kα excitation source ($h\nu$ = 1486.6 eV). The binding energies in XPS spectra were referenced with respect to the C 1s binding energy of adventitious carbon at 284.8 eV. Scanning electron microscopy (SEM) images were obtained on a Sirion 200 field emission scanning electron microanalyzer. Transmission electron microscopy (TEM) measurements were performed on JEOL-2010 and JEOL-2100F high resolution transmission electron microscopes.

2.3 Chemisorption and photocatalytic activity measurements

0.02 g of sample was added to 40 mL of dye aqueous solutions (MO and AO 7 concentrations: 400 mg/L; Rhodamine B (RhB) concentration: 10 mg/L). The suspension was well stirred in the dark and 3.5 mL aliquots of the aqueous solution were removed at regular intervals and centrifuged. The concentration of dye in the centrifuged aqueous solution was determined by measuring its absorption on a Shimadzu UV-2450 UV–vis spectrophotometer, from which the chemisorption capacity was calculated. After the system had reached the adsorption–desorption equilibrium of dye molecules on the catalyst surface, the suspension was illuminated by a 500 W Xe arc lamp (BL-GHX-CH500, Xi'an Depai Biotechnology Co. Ltd., China) positioned inside a cylindrical Pyrex vessel surrounded by a circulating water jacket to cool the lamp. A UV cutoff glass filter (λ > 420 nm) only allowing photons with wavelengths above 420 nm to pass was used between the Xe lamp and the tube containing the reaction suspension which was about 9 cm from the light source. 3.5 mL aliquots of aqueous solution were collected at regular intervals and centrifuged. The concentration of dye in the centrifuged aqueous solution was determined by measuring its absorption on a Shimadzu UV-2450 UV–vis spectrophotometer, from which the photocatalytic activity was calculated.

3. Results and discussion

3.1 Preparation and structures of Cu_2O–Au nanocomposites

The diffraction peaks in the XRD pattern of the as-prepared CuH sample (Fig. 1(a)) can all be indexed to hexagonal CuH (JCPDS file number 89-4182). The average crystallite size was calculated to be ~9 nm using the Debye–Scherrer equation. The corresponding TEM image (Fig. S-1, in the Electronic Supplementary Material (ESM)) shows that the as-prepared CuH

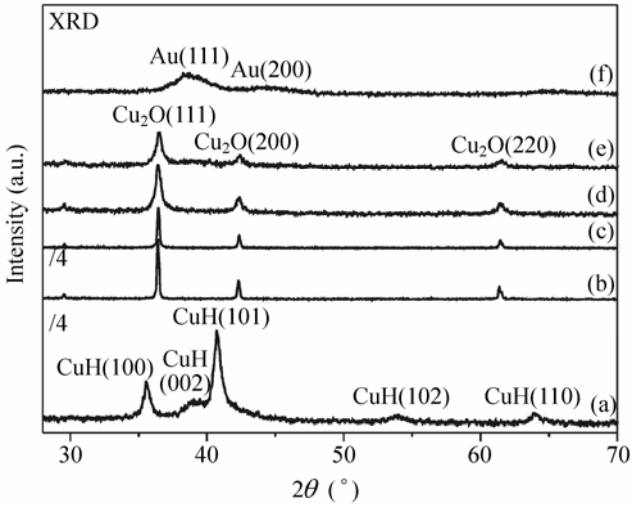

Figure 1 XRD patterns of CuH (a), Cu_2O–H_2O (b), Cu_2O–H_3O^+ (c), Cu_2O–Au-40 (d), Cu_2O–Au-20 (e), andCu_2O–Au-5 (f)

nanoparticles have a spindle shape (~10 nm × ~5 nm) and are seriously aggregated. Thus, the as-prepared CuH nanoparticles were dispersed in a PVP aqueous solution prior to further reaction. The CuH nanoparticles are not stable in aqueous solution at room temperature and slowly decompose, as evidenced by the formation of H_2 bubbles. The solid product of decomposition reaction is Cu_2O (denoted as Cu_2O–H_2O), as evidenced by the XRD pattern (Fig. 1(b), JCPDS file number 78-2076). The average crystallite size was calculated to be ~61 nm from the Debye–Scherrer equation. The SEM images (Figs. 2(a) and 2(b)) show that the Cu_2O nanoparticles are mostly large agglomerates while a few foil-like structures are also visible.

Interestingly, we found that addition of $HAuCl_4$ aqueous solution to the aqueous solution containing CuH nanoparticles greatly accelerated the rate of decomposition of CuH. The vigorous formation of H_2 bubbles was observed as soon as the $HAuCl_4$ aqueous solution was added and the time required for the complete decomposition of CuH was significantly shortened. The composition and morphology of the resulting solid product (Cu_2O–Au nanocomposites) denoted as Cu_2O–Au-x (where x represents the calculated Cu:Au molar ratio) depends on the value of x. Figures 1(d)–1(f) show the XRD patterns of Cu_2O–Au-40, Cu_2O–Au-20, and Cu_2O–Au-5, respectively. Cu_2O–Au-40 and Cu_2O–Au-20 exhibit the typical XRD pattern of Cu_2O and no obvious diffraction peaks of Au-related species could be observed. The average crystallite sizes of Cu_2O were calculated to be 20 and 18 nm in Cu_2O–Au-40 and Cu_2O–Au-20, respectively. In contrast, no obvious diffraction peaks of Cu_2O could be observed in the XRD pattern of Cu_2O–Au-5 and only broad diffraction peaks arising from Au (JCPDS file number 89-3697) appeared, whose average crystallite size was calculated be ~3 nm. The compositions of various Cu_2O–Au nanocomposites were analyzed by ICP-AES and the results are summarized in Table 1. It can be seen that the measured Cu:Au atomic ratio of Cu_2O–Au nanocomposites is lower than the calculated value.

Figure 3 shows the Cu 2p and Au 4f XPS spectra of various Cu_2O–Au nanocomposites. Au in all nanocomposites is metallic, as demonstrated by the Au $4f_{7/2}$ binding energy at 83.8 eV [43], and therefore, the absence of Au diffraction peaks in the XRD patterns of Cu_2O–Au-40 and Cu_2O–Au-20 implies that the size of Au nanoparticles in both Cu_2O–Au nanocomposites is beyond the detection limit of XRD. The Cu 2p XPS results reveal different copper oxidation states on the Cu_2O surface in different Cu_2O–Au nanocomposites. The Cu 2p XPS spectrum of Cu_2O–Au-40 consists of two components with Cu $2p_{3/2}$ binding energies at 935.4 and 933.7 eV that can be respectively assigned to $Cu(OH)_2$ and CuO [43]. This indicates that the surface of Cu_2O in Cu_2O–Au-40 is completely oxidized. A similar surface oxidation also occurs in Cu_2O–Au-20.

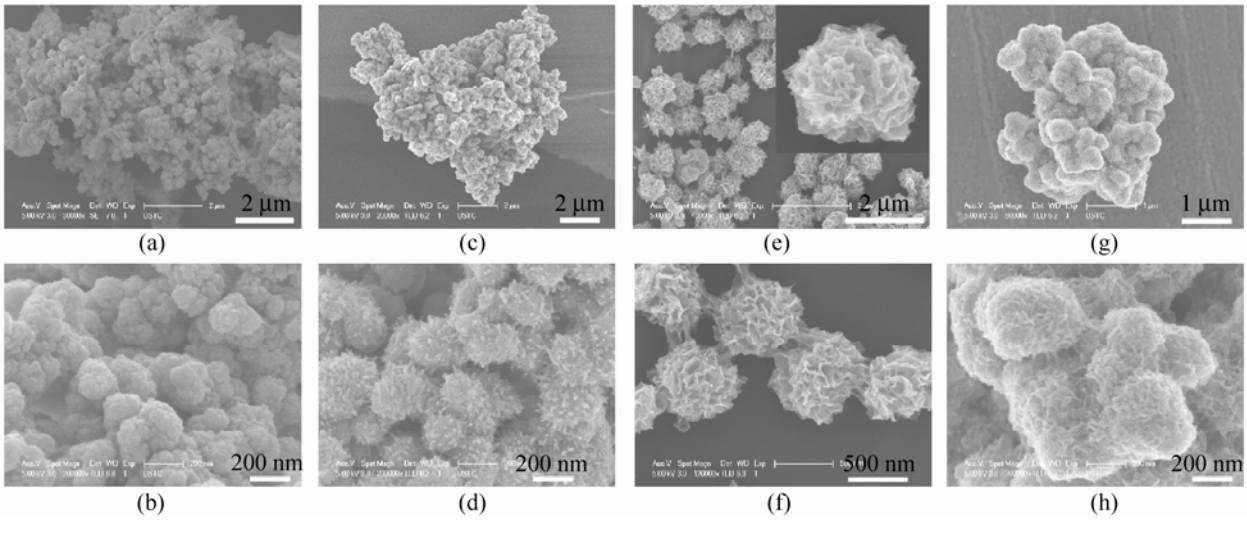

Figure 2 Representative SEM images of Cu_2O–H_2O (a & b), Cu_2O–Au-40 (c & d), Cu_2O–Au-20 (e & f), and Cu_2O–Au-5 (g & h)

Table 1 Cu:Au atomic ratios of Cu_2O–Au nanocomposites

Cu:Au atomic ratio	Cu_2O–Au-40	Cu_2O–Au-20	Cu_2O–Au-5
ICP-AES	33.11	14.04	1.36
XPS	31.15	18.02	11.56

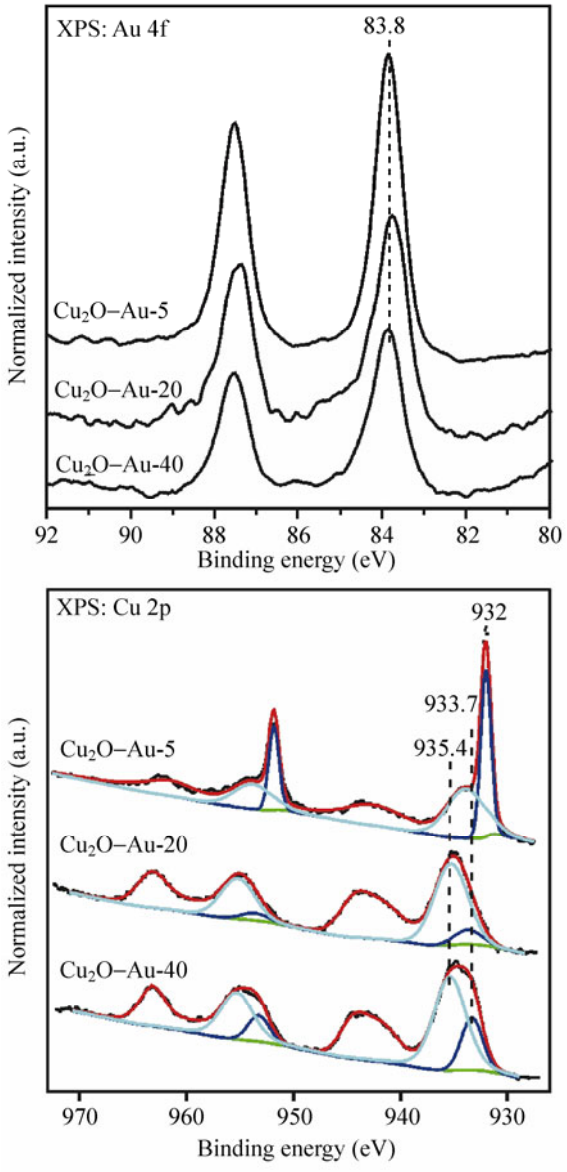

Figure 3 The Cu 2p and Au 4f XPS spectra of Cu_2O–Au-40, Cu_2O–Au-20, and Cu_2O–Au-5

However, the surface of Cu_2O in Cu_2O–Au-5 is only partially oxidized to CuO, as evidenced by the two components with Cu $2p_{3/2}$ binding energies at 933.9 and 932 eV that can be respectively assigned to CuO and Cu_2O [43], showing that Cu_2O in Cu_2O–Au-5 is less oxidized than in Cu_2O–Au-20 and Cu_2O–Au-40. Table 1 summarizes the surface Cu:Au atomic ratio of Cu_2O–Au nanocomposites as evaluated by XPS, which reflects the surface composition. The surface Cu:Au atomic ratios of Cu_2O–Au-20 and Cu_2O–Au-40 are similar to the bulk Cu:Au atomic ratios as determined by ICP-AES, but the surface Cu:Au atomic ratio of Cu_2O–Au-5 is much larger than the bulk Cu:Au atomic ratio, indicating that copper is greatly enriched in the surface region of Cu_2O–Au-5.

The SEM images demonstrate that Cu_2O–Au nanocomposites exhibit morphologies which depend on the Cu:Au ratio. Cu_2O–Au-40 consists of uniform spheres with many small particles protruding on the surface (Figs. 2(c) and 2(d)). The TEM image (Fig. 4(a)) demonstrates that the spheres are hollow. Thus nanoparticles in Cu_2O–Au-40 assemble into an echinus shape. The selected area electron diffraction (SAED) pattern (the inset in Fig. 4(a)) can be indexed to polycrystalline Cu_2O, but in the high-resloution transmission electron microscopy (HRTEM) image (Fig. 4(b)), lattice fringes between 2.14 and 2.18 Å from Cu_2O(200) and at 2.30 and 2.32 Å from Au(111) could all be observed, which reveals the presence of ultrafine Au colloids in the polycrystalline Cu_2O nanoparticles.

Strikingly, Cu_2O–Au-20 shows a beautiful and uniform flower-like morphology (Figs. 2(e) and 2(f)). The flower consists of curved thin petals with a size of ~500 nm. The TEM images (Figs. 5(a)–5(c)) demonstrate that curved thin petals extend from the pedicels. Very interestingly, the SAED patterns of the petal and pedicel areas of the flower-like Cu_2O–Au-20 nanocomposite (the insets in Fig. 5(b)) reveal that the pedicel areas contain polycrystalline Cu_2O (the diffraction ring arising from Cu_2O(111)) whereas the petal areas are amorphous. The dark-field STEM image (Fig. 5(d)) clearly shows that the contrasts between the petal and pedicel areas within an individual flower-like nanostructure vary considerably. The corresponding element mapping results (Figs. 5(e) and 5(f)) demonstrate that copper is distributed homogeneously within the nanostructure whereas there is no obvious Au signal. It should be noted that a pixel in the element mapping images corresponds to ~5 nm. Thus the bright contrast of the pedicel areas in the dark-field STEM image of the flower-like nanostructure arises from the good crystallinity, rather than from the heavy atom

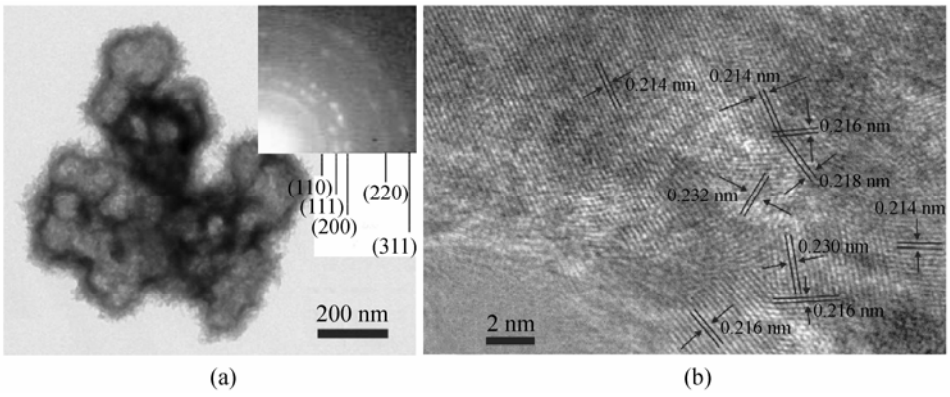

Figure 4 TEM (a) and HRTEM (b) images of Cu_2O–Au-40. The inset in (a) shows the ED pattern

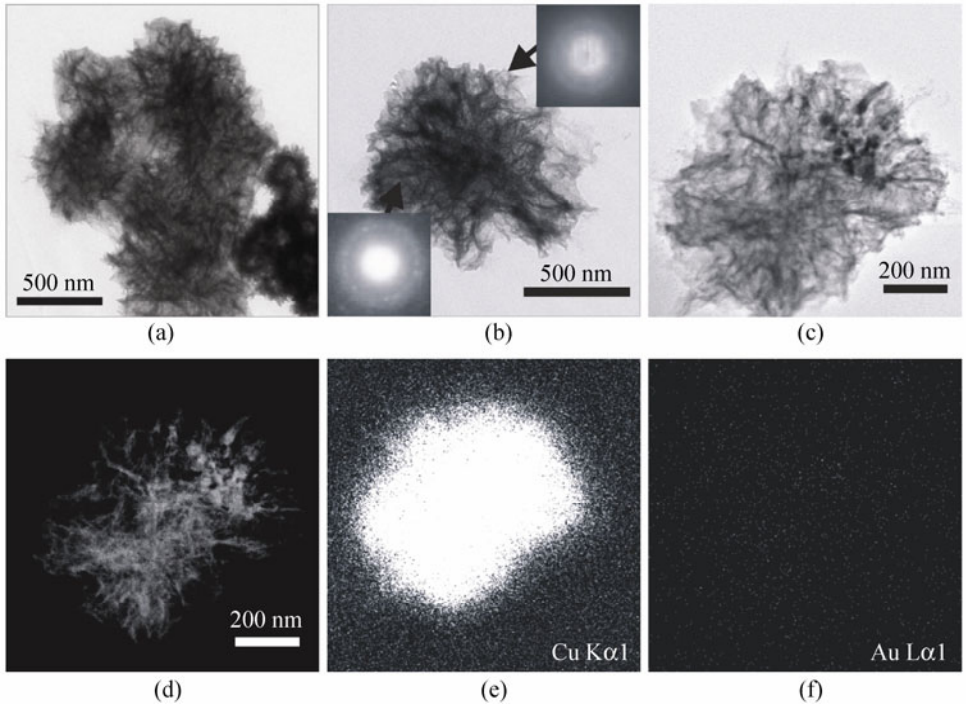

Figure 5 Representative TEM images of Cu_2O–Au-20 (a and b), the bright-field STEM image (c) and the dark-field STEM image (d) of an individual flower-like nanostructure of Cu_2O–Au-20 and the corresponding elemental mapping image of Cu (e) and Au (f); the insets in (b) show the SAED patterns of indicated areas

effect of Au, and the dark contrast of the petal areas in the dark-field STEM image of the flower-like nanostructure arises from their amorphous nature. The HRTEM images (Fig. 6) show a clearly visible Cu_2O(111) lattice fringe (~2.46 Å) in the pedicel areas, whereas no lattice fringe could be observed in the petal areas. The corresponding fast Fourier transform (FFT) images (insets in Fig. 6) also indicate that the pedicel area is crystalline whereas the petal area is not. Therefore, the flower-like nanostructure of Cu_2O–Au-20 consists of curved thin amorphous Cu_2O petals extending from polycrystalline Cu_2O pedicels. As far as we know, this is the first report of such a novel nanostructure for Cu_2O.

The SEM images (Figs. 2(g) and 2(h)) show that the nanostructures in Cu_2O–Au-5 consist of stacked thin foils. The corresponding TEM image (Fig. 7(a)) indicates that these nanostructures are porous or hollow. In

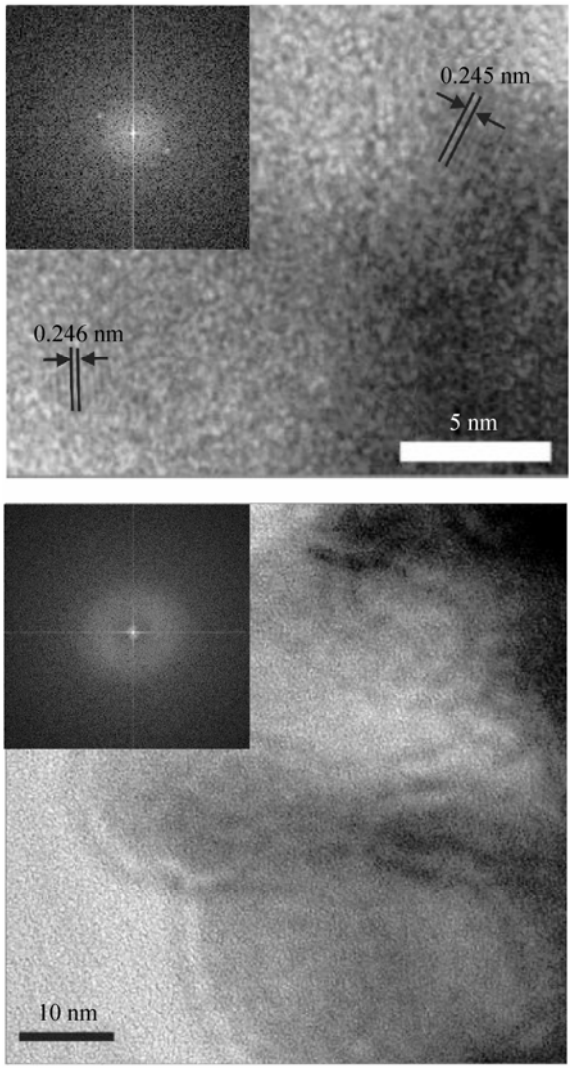

Figure 6 HRTEM image of the pedicel (upper) and TEM image of the petal (low) areas of Cu_2O–Au-20. The insets show the corresponding FFT images

contrast to Cu_2O–Au-40 and Cu_2O–Au-20, the SAED pattern (the inset in Fig. 7(a)) and the HRTEM image (Fig. 7(b)) of Cu_2O–Au-5 only demonstrates the presence of polycrystalline Au. However, the presence of copper in Cu_2O–Au-5 is shown by both ICP-AES and XPS and, moreover, the XPS results show that copper is greatly enriched on the surface of Cu_2O–Au-5 where the surface is only partially oxidized to CuO. This implies that Cu_2O in Cu_2O–Au-5 is amorphous and protected from surface oxidation. On basis of these data, we propose that the wall of the nanostructure in Cu_2O–Au-5 consists of Au colloids with underlying curved thin amorphous Cu_2O foils.

We also synthesized Cu_2O–Au-30 and Cu_2O–Au-10, whose SEM images are shown in Fig. S-2 (in the ESM). The morphology of Cu_2O–Au-30 is a mixture of those of Cu_2O–Au-40 and Cu_2O–Au-20, and the morphology of Cu_2O–Au-10 is a mixture of those of Cu_2O–Au-20 and Cu_2O–Au-5.

3.2 Formation mechanism of the Cu_2O–Au nanocomposites

The above results clearly show that the addition of $HAuCl_4$ aqueous solution can greatly affect the reaction of CuH nanoparticles in aqueous solution. The reaction of CuH alone in aqueous solution mainly leads to the formation of polycrystalline Cu_2O nanoparticles; after the addition of $HAuCl_4$ aqueous solution, amorphous Cu_2O foils form and their fraction in the product increases with decreasing Cu:Au ratio. Meanwhile, the nanoparticles in Cu_2O–Au-x assemble into different nanostructures depending on the value of x. First of all, the addition of $HAuCl_4$ aqueous solution changes the pH value of the CuH aqueous solution. We employed the HCl aqueous solution to adjust the pH value of the CuH aqueous solution to the same as that in the preparation of Cu_2O–Au-20 (pH = 5.0). The XRD pattern (Fig. 1(c)) demonstrates the formation of well-crystalline Cu_2O nanoparticles (denoted as Cu_2O–H_3O^+) with an average crystallite size of ~60 nm, and the SEM images (Fig. S-3, in the ESM) show that the morphology of Cu_2O–H_3O^+ is similar to that of Cu_2O–H_2O but with a larger fraction of curved thin amorphous Cu_2O foils. These results demonstrate that the pH value is not the main factor influencing the reaction of CuH in aqueous solution after addition of the $HAuCl_4$ aqueous solution.

The reaction process was monitored by measuring the UV–vis spectra of the aqueous solution at different reaction times. The results are presented in Fig. 8. We observed the appearance of two peaks at 540 and 780 nm in the UV–vis spectrum after the reaction proceeded for 5 min, whose intensity increased with the amount of $HAuCl_4$. The peak at 780 nm can be assigned to Cu(Ⅱ) in aqueous solution and the peak at 540 nm can be assigned to the surface plasmon resonance (SPR) of Au colloids [44]. These observations demonstrate that $[AuCl_4]^-$ reacts with CuH to form Cu(Ⅱ) and Au colloids. The Au colloidal particles are very fine and

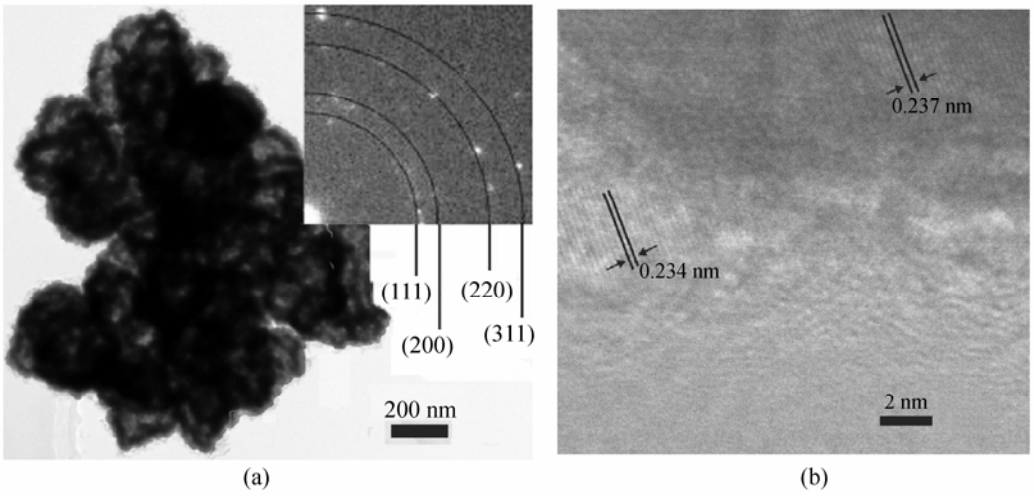

Figure 7 TEM (a) and HRTEM (b) images of Cu_2O–Au-5. The inset in (a) shows the ED pattern

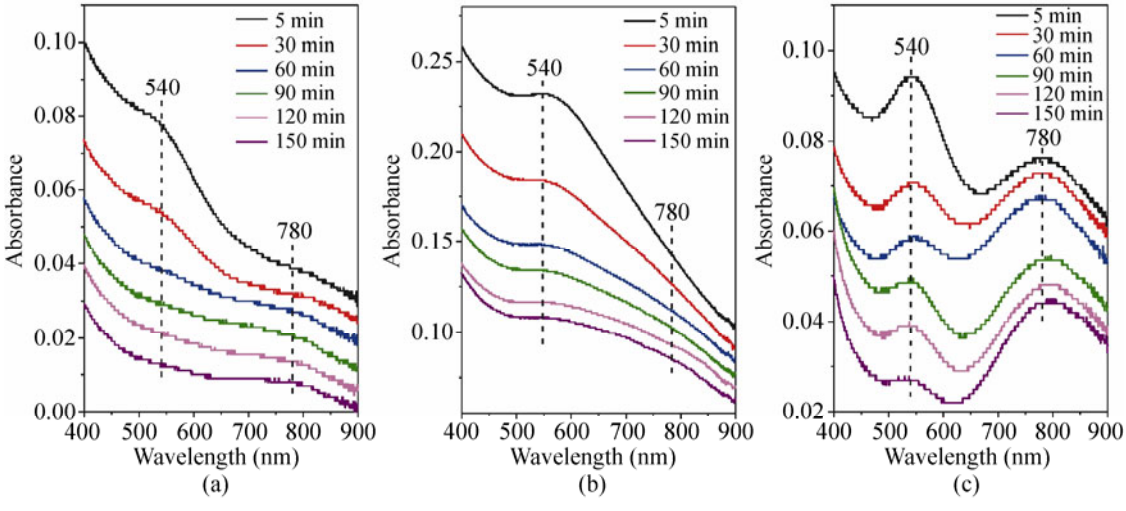

Figure 8 UV–vis spectra of the aqueous solution at the indicated reaction times during the course of the reactions for the preparation of Cu_2O–Au-40 (a), and Cu_2O–Au-20 (b), and Cu_2O–Au-5 (c)

cannot be removed from the aqueous solution by the centrifugation treatment employed in our experiments. As the reaction proceeded, the peak at 780 nm did not change, but the peak at 540 nm markedly decreased in intensity and did not change further after a reaction time of 60 min. This indicates that some Au colloids can subsequently deposit on the surface of the solid product in aqueous solution after their formation.

The morphology evolution of Cu_2O–Au-20 was investigated in detail by SEM (Fig. 9) because of its novelty. The solid product after reaction for 5 min consisted of spheres with many small particles attached on the surface. These attached small particles grew larger after reaction for 30 min and when the reaction time reached 60 min, curved thin foils were observed to evolve from the surface of the particles. The fraction of these curved thin foils in the solid product increased with the reaction time. The TEM image (Fig. S-4(a), in the ESM) shows that nanoparticles became seriously aggregated in the solid product after the reaction proceeded for 5 min. The corresponding HRTEM image (Fig. S-4(b), in the ESM) shows lattice fringes arising from CuH, Cu_2O, and Cu: lattice fringes at 2.52, 2.28, 2.17–2.23, and 1.42 Å from CuH (100), (002), (101), and (110), respectively; lattice fringes at 2.48, 2.11–2.15, and 1.26 Å from Cu_2O (111), (200), and (311), respectively; and lattice fringes of 2.02–2.08 and 1.83–1.86 Å from Cu (111) and (200), respectively.

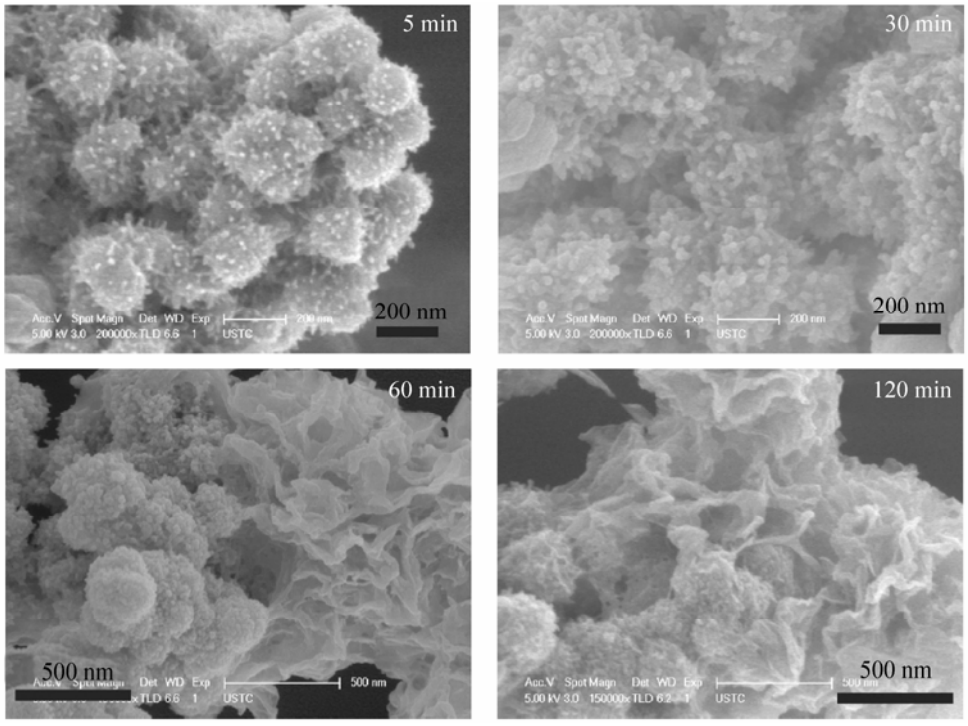

Figure 9 Representative SEM images of the solid products at the indicated reaction times during the course of the reaction for the preparation of Cu_2O–Au-20

The presence of Cu might arise from the electron radiation-induced decomposition of CuH under the vacuum conditions [42]. After the reaction proceeded for 60 min, nanoparticles in the solid product assembled into broken rings (Fig. S-4(c), in the ESM) and amorphous Cu_2O structures were visible extending from the surfaces of nanoparticles, consistent with the SEM image. The corresponding HRTEM image (Fig. S-4(d), in the ESM) shows that, in addition to the lattice fringes arising from CuH, Cu_2O, and Cu, lattice fringes arising from Au(111) (at 2.30–2.40 Å) are clearly visible. Meanwhile, the EDS analysis results show that the Cu:Au atomic ratio of the solid product decreased from 9.34 at 5 min to 0.37 at 60 min. These results also suggest the deposition of Au colloids on the surface of CuH nanoparticles during the reaction period between 5 and 60 min, in good agreement with the UV–vis spectroscopy measurements.

By correlating the composition and morphology of the solid products at different reaction times, it can be seen that the formation of curved thin foils of amorphous Cu_2O is closely associated with the deposition of Au colloids on the surface of CuH nanoparticles. The decomposition of CuH in aqueous solution leads to the formation of polycrystalline Cu_2O and H_2. We propose that Au colloids can catalyze the decomposition of CuH in aqueous solution. Because of the enhanced rate of CuH decomposition catalyzed by Au colloids, the formation rate of H_2 is greatly accelerated, which drives the simultaneous formation of amorphous Cu_2O. Therefore, the following chemical reactions in the CuH + $HAuCl_4$ aqueous solution can be postulated:

$$6\,CuH(s) + 4[AuCl_4]^- \longrightarrow 6Cu^{2+} + 16Cl^- + 4Au(s) + 3H_2(g) \quad (1)$$

$$2\,CuH(s) + H_2O \longrightarrow Cu_2O\,(s, \text{polycrystalline}) + 2H_2(g) \quad (2)$$

$$2\,CuH\,(s) + H_2O \xrightarrow{Au} Cu_2O\,(s, \text{amorphous}) + 2H_2(g) \quad (3)$$

Meanwhile, the H_2 bubbles might also serve as a template for the assembly of nanoparticles [45, 46].

On basis of the above experimental results and discussion, we propose the following mechanism for the formation of Cu_2O–Au-20: $[AuCl_4]^-$ reacts with CuH to form Au colloids that subsequently deposit on the surface of CuH nanoparticles and catalyze the decomposition of CuH nanoparticles; the rapidly-generated H_2 bubbles do not allow the simultaneously-formed Cu_2O to crystallize and result in the formation of curved thin foils of amorphous Cu_2O; they might also act as a template to assemble the amorphous Cu_2O curved thin foils into flower-like nanostructures; meanwhile, some CuH nanoparticles not in contact with Au colloids undergo a slower noncatalytic decomposition forming polycrystalline Cu_2O nanoparticles that, together with Au colloids, become embedded into the flower-like nanostructures. This mechanism can also explain the Cu:Au atomic ratio-dependent morphology of Cu_2O–Au nanocomposites. For Cu_2O–Au-40, because of the limited numbers of Au colloidal particles, most CuH nanoparticles undergo the noncatalytic decomposition forming polycrystalline Cu_2O nanoparticles that are directed by the H_2 bubbles to assemble into hollow nanostructures; the Au colloids and amorphous Cu_2O are located on the surface of hollow nanostructures consisting of polycrystalline Cu_2O nanoparticles. For Cu_2O–Au-5, because of their large number, Au colloidal particles can cover almost the entire surfaces of the CuH nanoparticles and all the CuH nanoparticles undergo the catalytic decomposition to form curved thin foils of amorphous Cu_2O that, together with Au nanoparticles, assemble into hollow nanostructures.

3.3 Chemisorption and photocatalytic activity of Cu_2O–Au nanocomposites

We have also studied the performance of our Cu_2O–Au nanocomposites in the visible-light-driven photocatalytic degradation of various dye molecules (Fig. 10). The corresponding UV–vis absorption spectra during the chemisorption and photodegradation processes are

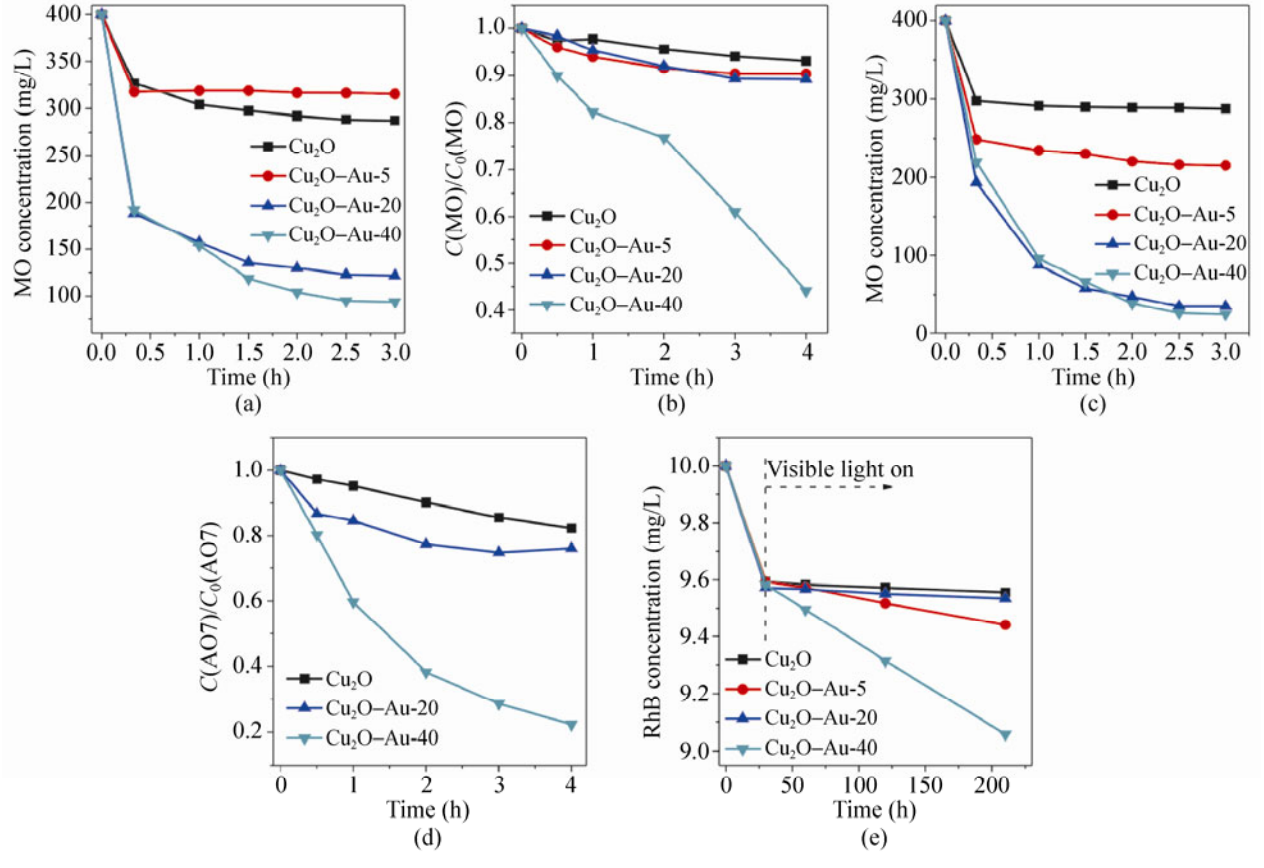

Figure 10 The chemisorption and visible-light-driven (λ > 420 nm) photodegradation activity of Cu_2O–Au nanocomposites toward MO (a & b), AO 7 (c & d), and Rhodamine B (e). C_0 represents the concentration after reaching the chemisorption equilibrium in the darkness

shown in Figs. S-5–S-7 (in the ESM). We found that the chemisorption behaviors of Cu_2O–Au nanocomposites in the dark are interesting. Table 2 summarizes the chemisorption capacities of Cu_2O–Au nanocomposites towards various dye molecules, clearly demonstrating that the chemisorption capacity of Cu_2O–Au nanocomposites depends on their composition and the type of dye molecule. Cu_2O and Cu_2O–Au nanocomposites exhibit remarkable chemisorption capacities toward MO and AO 7; however, they only chemisorb RhB, methylene blue (results not shown) and *p*-nitrophenol (results not shown) very slightly. The chemisorption capacity toward MO and AO 7 increases greatly from Cu_2O to Cu_2O–Au-40, and then decreases with the further decrease of the Cu:Au atomic ratio in the Cu_2O–Au nanocomposite. The largest chemisorption capacities reached 612 and 751 mg/g(Cu_2O–Au-40) for MO and AO 7, respectively. Figure S-8 (in the ESM) shows the N_2 adsorption-desorption isotherms of Cu_2O and Cu_2O–Au nanocomposites, from which their BET surface area, average pore size and pore volume were calculated and summarized in Table 2. The BET surface area increases with decreasing Cu:Au atomic ratio. This implies that Cu_2O is the active component for the chemisorption of MO and AO 7. As demonstrated in Table 2, compared with that of Cu_2O, the BET surface area of Cu_2O–Au-40 (12.4 m^2/g) cannot solely account for its large chemisorption capacity; moreover, by normalizing the chemisorption capacity with the content of Cu_2O in the Cu_2O–Au nanocomposites, it can be deduced that the specific chemisorption activity of Cu_2O in Cu_2O–Au nanocomposites increases with decreasing Cu:Au atomic ratio. Therefore, amorphous Cu_2O might be more active in the chemisorption of MO and AO 7 than crystalline Cu_2O, but it cannot be ruled out that a synergetic effect between Au and Cu_2O occurs in the chemisorption of MO and AO 7 on Cu_2O–Au nanocomposites.

The structure of the adsorbate affects the chemisorption performance of Cu_2O–Au nanocomposites. Cu_2O–Au nanocomposites chemisorb MO and AO 7, but not RhB, methylene blue and *p*-nitrophenol. The structures of these dye molecules are shown in Fig. S-9 (in the ESM). Figure 11 shows the infrared spectra of

Table 2 Structural parameters, chemisorption capacities and photocatalytic reaction rate constants of Cu_2O–Au nanocomposites

Sample	BET surface area (m^2/g)	Average pore size (nm)	Pore volume (cm^3/g)	Chemisorption capacity ($mg/g_{catalyst}$)			Photocatalytic reaction rate constant (10^{-4}/min)		
				MO	AO 7	RhB	MO	AO 7	RhB
Cu_2O	7.8	17.4	0.05	227	224	0.81	2.79	8.21	0.21
Cu_2O–Au-40	12.4	18.7	0.09	612	751	0.83	31.5	63.5	3.15
Cu_2O–Au-20	24.5	18.6	0.16	556	730	0.85	6.42	14.7	0.23
Cu_2O–Au-5	37.0	10.8	0.16	169	369	0.81	5.26	–	0.91

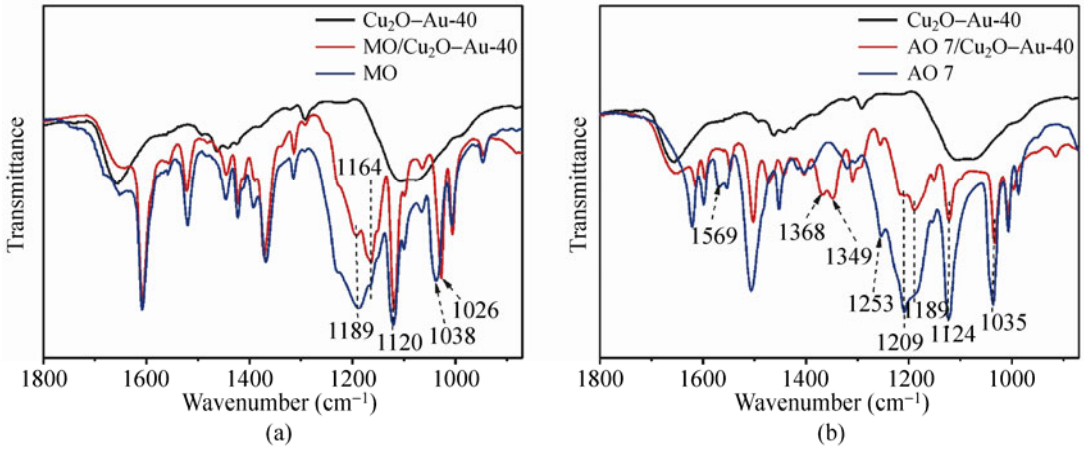

Figure 11 Infrared spectra of MO and AO 7molecules adsorbed on Cu_2O–Au-40

MO and AO 7 chemisorbed on Cu_2O–Au-40. The pure Cu_2O–Au-40 exhibits O–O (from adsorbed O_2^-) and Cu–O vibrational bands at 1088 and 624 cm^{-1} (spectrum not shown), respectively [47]; other vibrational bands observed between 1349 and 1520 cm^{-1} and at 1658 cm^{-1} might arise from PVP and hydroxyl groups on the surface of pure Cu_2O–Au-40. After the chemisorption of MO, the bands from Cu_2O–Au-40 are strongly quenched; instead, vibrational bands similar to those of pure MO are clearly visible, evidencing the strong chemisorption of MO on Cu_2O–Au-40. Upon chemisorption, the relative peak intensities of the vibrational bands of MO change significantly. The most obvious changes occur for the $\nu_s(SO_3^-)$ vibrational bands (1189 and 1164 cm^{-1}) and the $\nu_{as}(SO_3^-)$ vibrational bands (1120 and 1038 cm^{-1}). The band at 1189 cm^{-1} is stronger than that at 1164 cm^{-1} for pure MO, whereas the reverse is true for chemisorbed MO; moreover, the $\nu_{as}(SO_3^-)$ vibrational band shifts from 1038 cm^{-1} for pure MO to 1026 cm^{-1} after MO chemisorption. These results suggest that chemisorbed MO interacts with Cu_2O via its SO_3^- group. The situation is different for AO 7. The presence of ν(C=O) (1569 cm^{-1}) and ν(C–N) (1253 cm^{-1}) vibrational bands for pure AO 7 suggest [48] that AO 7 is in the hydrazone form (Fig. S-9, in the ESM). After chemisorption, the ν(C=O) band disappears and the ν(C–N) band is attenuated greatly, and two new vibrational peaks appear at 1368 and 1349 cm^{-1} that can be assigned to ν(N=N) and ν(C–O) [49]. This suggests that chemisorbed AO 7 is in the azo form (Fig. S-9, in the ESM). We found that the vibrational bands arising from the SO_3^- group in AO 7 do not change upon chemisorption except that the relative intensities of bands at 1209 and 1189 cm^{-1} are reversed for pure and chemisorbed AO 7. Instead, the aromatic C=C stretching vibration bands (1622, 1599, 1482 and 1454 cm^{-1}) [50] are all shifted downwards by several wavenumbers after chemisorption. Therefore, we propose that AO chemisorbs on Cu_2O–Au-40 with the O atom in the C=O group interacting with Cu(I), with its benzene ring lying down on the surface, and that the SO_3^- group does not contribute to the chemisorption.

Cu_2O and Cu_2O–Au nanocomposites show activity in the visible-light-driven photodegradation of MO, AO 7, and RhB (Figs. 10(b), 10(d) and 10(e)). Assuming that the photocatalytic reaction follows first-order kinetics, the photocatalytic reaction rate constants were calculated (Fig. S-10 in the ESM) and are summarized in Table 2. The reaction rate constant of the photodegradation reaction decreases the order: AO 7 > MO ≫ RhB, in agreement with the order of the chemisorption and activation of these dye molecules on the photocatalyst. Cu_2O–Au-40 is more active than Cu_2O by about one order, but Cu_2O–Au-20 and Cu_2O–Au-5 have similar activities to Cu_2O. Cu_2O–Au-5 does not exhibit any activity in the photodegradation of AO 7. It has been argued that Cu_2O cannot catalyze photocatalytic reactions via the direct photocatalytic mechanism [7–9, 16, 38]. Cu_2O nanocrystals have been reported to be inactive in the photodegradation of dye molecules under visible light irradiation, but very active in the presence of H_2O_2 [16, 38]. de Jongh et al. [7] reported that Cu_2O is not an effective photocatalyst for water splitting but could reduce dissolved oxygen to H_2O_2, and Shi et al. [16] recently proposed that the formation of H_2O_2 in this way is responsible for the photodegradation of dye molecules over Cu_2O. Meanwhile, involvement of the so-called semiconductor-mediated photodegradation (SMPD) mechanism [50], in which absorption of light by the chemisorbed dye molecule generates an excited state from which it injects an electron into the conduction band of a semiconductor and is thereby oxidized, cannot be ruled out. The underlying photocatalytic mechanism needs further investigation, but we consider the following factors contribute to the high photocatalytic activity of the Cu_2O–Au-40 nanocomposite: (1) its large chemisorption capacity; (2) the amount and structure of Au colloids contained in Cu_2O–Au-40 are appropriate; (3) the surface of Cu_2O in Cu_2O–Au-40 is completely oxidized to CuO and $Cu(OH)_2$, and thus there exist Au–Cu_2O–CuO hetero-junctions in Cu_2O–Au-40 that can act to effectively inhibit the recombination process of photo-induced electrons and holes, as previously proposed for Pt/RuO_2/TiO_2 photocatalysts [51]. The formation of Cu_2O–Au [36, 37] and CuO–Cu_2O [38] nanocomposites has previously been reported to enhance the photocatalytic activity of Cu_2O in the photodegradation of dye molecules. Considering both chemisorption and visible-light-driven photodegradation, 20 mg of Cu_2O–Au-40 gives decolorization

efficiencies of 98.6% for AO 7 and 89.7% for MO with an initial dye concentration of 400 mg/L, demonstrating that Cu_2O–Au-40 is a promising chemisorption–photocatalysis integrated catalyst.

4. Conclusions

We report for the first time the synthesis of novel Cu_2O–Au nanocomposites by the decomposition of CuH nanoparticles in aqueous solution catalyzed by Au colloids. Depending on the Au:Cu ratio, Cu_2O–Au nanocomposites exhibit a variety of novel nanostructures including a beautiful flower-like nanostructure that consist of polycrystalline Cu_2O, amorphous Cu_2O and Au colloids. We propose that the H_2 bubbles rapidly generated during the course of the catalytic decomposition reaction induce the simultaneously-formed Cu_2O to grow as amorphous curved thin foils and may also act as a template for the formation of the novel nanostructures. Cu_2O–Au-40 exhibits remarkable chemisorption capacity and visible-light-driven photocatalytic activity toward MO and AO 7, and thus is a chemisorption–photocatalysis integrated catalyst. We believe that the use of catalytic decomposition of a metal hydride opens up a new approach for the fabrication of other metal/metal oxide nanocomposites with novel nanostructures and properties.

Acknowledgements

This work was financially supported by the National Natural Science Foundation of China (grant No. 20773113), the Solar Energy Project of the Chinese Academy of Sciences, the National Basic Research Program of China (No. 2010CB923302), MOE program for PCSIRT (IRT0756), the Fundamental Research Funds for the Central Universities (No. WK2060030005), and the MPG–CAS partner group program.

Electronic Supplementary Material: Supplementary material giving additional details of characterization of the materials and photodegradation of the dyes is available in the online version of this article at http://dx.doi.org/ 10.1007/s12274-011-0151-8.

References

[1] Shen, M. Y.; Yokouchi, T.; Koyama, S.; Goto, T. Dynamics associated with Bose–Einstein statistics of orthoexcitons generated by resonant excitations in cuprous oxide. *Phys. Rev. B* **1997**, *56*, 13066–13072.

[2] Rai, B. P. Cuprous oxide solar cells: A review. *Solar Cells* **1988**, *25*, 265–272.

[3] Zhang, J.; Liu, J.; Peng, Q.; Wang, X.; Li, Y. Nearly monodisperse Cu_2O and CuO nanospheres: Preparation and applications for sensitive gas sensors. *Chem. Mater.* **2006**, *18*, 867–871.

[4] Poizot, P.; Laruelle, S.; Grugeon, S.; Dupont, L.; Taracon, J. M. Nano-sized transition-metal oxides as negative-electrode materials forlithium-ion batteries. *Nature* **2000**, *407*, 496–499.

[5] Bao, H. Z.; Zhang, W. H.; Shang, D. L.; Hua, Q.; Ma, Y. S.; Jiang, Z. Q.; Yang, J. L.; Huang, W. X. Shape-dependent reducibility of cuprous oxide nanocrystals. *J. Phys. Chem. C* **2010**, *114*, 6676–6680.

[6] Hara, M.; Kondo, T.; Komoda, M.; Ikeda, S.; Shinohara, K.; Tanaka, A.; Kondo, J. N.; Domen, K. Cu_2O as a photocatalyst for overall water splitting under visible light irradiation. *Chem. Commun.* **1998**, 357–358.

[7] de Jongh, P. E.; Vanmaekelbergh, D.; Kelly, J. J. Cu_2O: A catalyst for the photochemical decomposition of water? *Chem. Commun.* **1999**, 1069–1070.

[8] Hara, M.; Komoda, M.; Hasei, H.; Yashima, M.; Ikeda, S.; Takata, T.; Kondo, J. N.; Domen, K. A study of mechano-catalysts for overall water splitting. *J. Phys. Chem. B* **2000**, *104*, 780–785.

[9] Walker, A. V.; Yates, J. T. Jr. Does cuprous oxide photosplit water? *J. Phys. Chem. B* **2000**, *104*, 9038–9043.

[10] Kuo, C. -H.; Huang, M. H. Facile synthesis of Cu_2O nanocrystals with systematic shape evolution from cubic to octahedral structures. *J. Phys. Chem. C* **2008**, *112*, 18355–18360.

[11] Zhang, D. -F.; Zhang, H.; Guo, L.; Zheng, K.; Han, X. -D.; Zhang, Z. Delicate control of crystallographic facet-oriented Cu_2O nanocrystals and the correlated adsorption ability. *J. Mater. Chem.* **2009**, *19*, 5220–5225.

[12] Ho, J. Y.; Huang, M. H. Synthesis of submicrometer-sized Cu_2O crystals with morphological evolution from cubic to hexapod structures and their comparative photocatalytic activity. *J. Phys. Chem. C* **2009**, *113*, 14159–14164.

[13] Zheng, Z.; Huang, B.; Wang, Z.; Guo, M.; Qin, X.; Zhang, X.; Wang, P.; Dai, Y. Crystal faces of Cu_2O and their stabilities in photocatalytic reactions. *J. Phys. Chem. C* **2009**, *113*, 14448–14453.

[14] Zhang, Y.; Deng, B.; Zhang, T. R.; Dao, D. M.; Xu, A. W. Shape effects of Cu_2O polyhedral microcrystals on photocatalytic activity. *J. Phys. Chem. C* **2010**, *114*, 5073–5079.

[15] Xu, H.; Wang, W.; Zhu, W. Shape evolution and size-controllable synthesis of Cu_2O octahedra and their morphology-dependent photocatalytic properties. *J. Phys. Chem. B* **2006**, *110*, 13829–13834.

[16] Shi, J.; Huang, X.; Tan, Y. Synthesis and enhanced photocatalytic activity of regularly shaped Cu_2O nanowire polyhedra. *Nano Res.* **2011**, *4*, 448–459.

[17] Ng, C. H. B.; Fan, W. Y. Shape evolution of Cu_2O nanostructures via kinetic and thermodynamic controlled growth. *J. Phys. Chem. B* **2006**, *110*, 20801–20807.

[18] Kuo, C. -H.; Chen, C. -H.; Huang, M. H. Seed-mediated synthesis of monodispersed Cu_2O nanocubes with five different size ranges from 40 to 420 nm. *Adv. Funct. Mater.* **2007**, *17*, 3773–3780.

[19] Gou, L.; Murphy, C. J. Solution-phase synthesis of Cu_2O nanocubes. *Nano. Lett.* **2003**, *3*, 231–234.

[20] Siegfried, M. J.; Choi, K. -S. Directing the architecture of cuprous oxide crystals during electrochemical growth. *Angew. Chem. Int. Ed.* **2005**, *44*, 3218–3223.

[21] Siegfried, M. J.; Choi, K. -S. Electrochemical crystallization of cuprous oxide with systematic shape evolution. *Adv. Mater.* **2004**, *16*, 1743–1746.

[22] Li, H.; Liu, R.; Zhao, R.; Zheng, Y.; Chen, W.; Xu, Z. Morphology control of electrodeposited Cu_2O crystals in aqueous solutions using room temperature hydrophilic ionic liquids. *Cryst. Growth Des.* **2006**, *6*, 2795–2798.

[23] Lu, C.; Qi, L.; Yang, J.; Wang, X.; Zhang, D.; Xie, J.; Ma, J. One-pot synthesis of octahedral Cu_2O nanocages via a catalytic solution route. *Adv. Mater.* **2005**, *17*, 2562–2567.

[24] Teo, J. J.; Chang, Y.; Zeng, H. C. Fabrications of hollow nanocubes of Cu_2O and Cu via reductive self-assembly of CuO nanocrystals. *Langmuir* **2006**, *22*, 7369–7377.

[25] Chang, Y.; Teo, J. J.; Zeng, H. C. Formation of colloidal CuO nanocrystallites and their spherical aggregation and reductive transformation to hollow Cu_2O nanospheres. *Langmuir* **2005**, *21*, 1074–1079.

[26] Xu, H.; Wang, W. Template synthesis of multishelled Cu_2O hollow spheres with a single-crystalline shell wall. *Angew. Chem. Int. Ed.* **2007**, *46*, 1489–1492.

[27] Pan, M. L.; Zeng, H. C. Highly ordered self-assemblies of submicrometer Cu_2O spheres and their hollow chalcogenide derivatives. *Langmuir* **2010**, *26*, 5963–5970.

[28] Kuo, C. -H.; Huang, M. H. Fabrication of truncated rhombic dodecahedral Cu_2O nanocages and nanoframes by particle aggregation and acidic etching. *J. Am. Chem. Soc.* **2008**, *130*, 12815–12820.

[29] Sui, Y.; Fu, W.; Zeng, Y.; Yang, H.; Zhang, Y.; Chen, H.; Li, Y.; Li, M.; Zou, G. Synthesis of Cu_2O nanoframes and nanocages by selective oxidative etching at room temperature. *Angew. Chem. Int. Ed.* **2010**, *49*, 4282–4285.

[30] Singh, D. P.; Neti, N. R.; Sinha, A. S. K.; Srivastava, O. N. Growth of different nanostructures of Cu_2O (nanothreads, nanowires, and nanocubes) by simple electrolysis based oxidation of copper. *J. Phys. Chem. C* **2007**, *111*, 1638–1645.

[31] Wang, W.; Wang, G.; Wang, X.; Zhan, Y.; Liu, Y.; Zheng, C. Synthesis and characterization of Cu_2O nanowires by a novel reduction route. *Adv. Mater.* **2002**, *14*, 67–69.

[32] Tan, Y.; Xue, X.; Peng, Q.; Zhao, H.; Wang, T.; Li, Y. Controllable fabrication and electrical performance of single crystalline Cu_2O nanowires with high aspect ratios. *Nano. Lett.* **2007**, *7*, 3723–3728.

[33] Hong, X.; Wang, G.; Zhu, W.; Shen, X.; Wang, Y. Synthesis of sub-10 nm Cu_2O nanowires by poly(vinyl pyrrolidone)-assisted electrodeposition. *J. Phys. Chem. C* **2009**, *113*, 14172–14175.

[34] Yuhas, B. D.; Yang, P. Nanowire-based all-oxide solar cells. *J. Am. Chem. Soc.* **2009**, *131*, 3756–3761.

[35] Kuo, C. -H.; Huang, M. H. Morphologically controlled synthesis of Cu_2O nanocrystals and their properties. *Nano Today* **2010**, *5*, 106–116.

[36] Kuo, C. H.; Hua, T. E.; Huang, M. H. Au nanocrystal-directed growth of Au–Cu_2O core–shell heterostructures with precise morphological control. *J. Am. Chem. Soc.* **2009**, *131*, 17871–17878.

[37] Kuo, C. H.; Yang, Y. C.; Gwo, S.; Huang, M. H. Facet-dependent and Au nanocrystal-enhanced electrical and photocatalytic properties of Au–Cu_2O core–shell heterostructures. *J. Am. Chem. Soc.* **2011**, *133*, 1052–1057.

[38] Hu, H.; Yu, J.; Liu, S.; Mann, S. Template-free hydrothermal synthesis of CuO/Cu_2O composite hollow microspheres. *Chem. Mater.* **2007**, *19*, 4327–4334.

[39] Zhang, Y. G.; Ma, L. L.; Li, J. L.; Yu, Y. *In situ* Fenton reagent generated from TiO_2/Cu_2O composite film: A new way to utilize TiO_2 under visible light irradiation. *Environ. Sci. Technol.* **2007**, *41*, 6264–6269.

[40] Li, J. L.; Liu, L.; Yu, Y.; Tang, Y. W.; Li, H. L.; Du, F. P. Preparation of highly photocatalytic active nano-size TiO_2–Cu_2O particle composites with a novel electrochemical method. *Electrochem. Commun.* **2004**, *6*, 940–943.

[41] Lalitha, K.; Sadanandam, G. Kumari, V. D.; Subrahmanyam, M.; Sreedhar, B.; Hebalkar, N. Y. Highly stabilized and finely dispersed Cu_2O/TiO_2: A promising visible sensitive photocatalyst for continuous production of hydrogen from

glycerol:water mixtures. *J. Phys. Chem. C* **2010**, *114*, 22181–22189.

[42] Goedkoop, J. A.; Andresen, A. F. The crystal structure of copper hydride. *Acta Crystallogr.* **1955**, *8*, 118–119.

[43] Moulder, T. F.; Stickle, W. F.; Sobol, P. E.; Bomben, K. D. *Handbook of X-ray Photoelectron Spectroscopy;* Perkin Elmer: Eden Prairie, Minnesota, 1992.

[44] Kelly, K. L.; Coronado, E.; Zhao, L. L.; Schatz, G. C. The optical properties of metal nanoparticles: The influence of size, shape, and dielectric environment. *J. Phys. Chem. B* **2003**, *107*, 668–677.

[45] Tong, G.; Guan, J.; Xiao, Z.; Mou, F.; Wang, W.; Yan, G. *In situ* generated H_2 bubble-engaged assembly: A one-step approach for shape-controlled growth of Fe nanostructures. *Chem. Mater.* **2008**, *20*, 3535–3539.

[46] Hua, Q.; Huang, W. X. Chemical etching induced shape change of magnetite microcrystals. *J. Mater. Chem.* **2008**, *18*, 4286–4290.

[47] Nagase, K.; Zheng, Y.; Kodama, Y. Kakuta, J. Dynamic study of the oxidation state of copper in the course of carbon monoxide oxidation over powdered CuO and Cu_2O. *J. Catal.* **1999**, *187*, 123–130.

[48] Bauer, C.; Jacques, P.; Kalt, A. Investigation of the interaction between a sulfonated azo dye (AO7) and a TiO_2 surface. *Chem. Phys. Lett.* **1999**, *307*, 397–406.

[49] Saito, Y.; Kim, B.; Machida, K.; Uno, T. The coordinative behavior of the ethereal oxygen atom in cobalt, nickel and copper complexes with Schiff bases obtained from salicylaldehyde derivatives and 2-(aminomethyl)furan. *Bull. Chem. Soc. Jpn.* **1974**, *47*, 2111–2114.

[50] Chen, C.; Ma, W.; Zhao, J. Semiconductor-mediated photo-degradation of pollutants under visible-light irradiation. *Chem. Soc. Rev.* **2010**, *39*, 4206–4219.

[51] Hoffmann, M. R.; Martin, S. T.; Choi, W.; Bahnemann, D. W. Environmental applications of semiconductor photocatalysis. *Chem. Rev.* **1995**, *95*, 69–96.